

# Toward an Earth Clouds, Aerosols and Radiation Explore (EarthCARE) thermal flux determination: Evaluation using Clouds and the Earth's Radiant Energy System (CERES) true along-track data

C. Domenech,<sup>1</sup> T. Wehr,<sup>2</sup> and J. Fischer<sup>1</sup>

Received 18 October 2010; revised 16 December 2010; accepted 30 December 2010; published 29 March 2011.

[1] The Earth Clouds, Aerosols and Radiation Explorer (EarthCARE) mission developed by the European Space Agency and the Japan Aerospace Exploration Agency addresses the need to improve the understanding of the interactions between cloud, aerosol, and radiation processes. The broadband radiometer (BBR) instrument on board the EarthCARE spacecraft provides measurements of broadband reflected solar and emitted thermal radiances at the top of atmosphere (TOA) over the along-track satellite path at three fixed viewing zenith angles. The multiangular information provided by the BBR, combined with the spectral information from the EarthCARE's multispectral imager (MSI) can be exploited to construct accurate thermal radiance-to-flux conversion algorithms on the basis of radiative transfer modeling. In this study, the methodology to derive longwave (LW) fluxes from BBR and MSI data is described, and the performance of the LW BBR angular models is compared with the Clouds and the Earth's Radiant Energy System (CERES) Terra flux retrievals in order to evaluate the reliability of the BBR synthetic models when applied to satellite-based radiances. For this purpose, the BBR methodology proposed in this work is adapted to the CERES and the Moderate Resolution Imaging Spectroradiometer (MODIS) instrument specifications, and new LW angular models for CERES are developed. According to plane-parallel simulations, the BBR LW flux uncertainty caused by flux inversion could be reduced up to  $0.4 \text{ W m}^{-2}$ . The intercomparison between CERES BBR-like adapted and CERES original angular models is performed over a BBR-like database of CERES true along track, and the averaged instantaneous retrievals agree to within  $2 \text{ W m}^{-2}$ .

**Citation:** Domenech, C., T. Wehr, and J. Fischer (2011), Toward an Earth Clouds, Aerosols and Radiation Explore (EarthCARE) thermal flux determination: Evaluation using Clouds and the Earth's Radiant Energy System (CERES) true along-track data, *J. Geophys. Res.*, 116, D06115, doi:10.1029/2010JD015212.

## 1. Introduction

[2] The Earth Clouds, Aerosols and Radiation Explorer (EarthCARE) mission [European Space Agency, 2004] is a joint European-Japanese scientific collaboration addressing the need for a better understanding of the interactions between cloud, radiative and aerosol processes that play a critical role in climate regulation and the radiative balance of the Earth. The mission scientific goals will be achieved with two active and two passive instruments on board the same spacecraft. In particular, the atmospheric lidar (ATLID) and the cloud profiling radar (CPR) will retrieve vertical profiles of aerosols and clouds and the broadband radiometer (BBR)

and the multispectral imager (MSI) will measure broadband (BB) and narrowband (NB) radiances at the top of atmosphere (TOA). The EarthCARE payload and the instrument observation geometry are shown in Figure 1. The BBR will measure the TOA radiance along track (AT) with a sampling along the satellite's flight direction in three fixed directional views (nadir and forward/backward at  $50^\circ$ ) over the same footprint of  $10 \times 10 \text{ km}$  to derive radiative fluxes,  $F(\text{W m}^{-2})$ , from reflected shortwave (SW) and emitted longwave (LW) radiation,  $L(\text{W m}^{-2} \text{ sr}^{-1})$ , emerging from the same atmospheric region where the active sensors also acquire measurements of cloud and aerosol profiles. With this approach, the BB measurements provide the boundary condition for the flux calculations under consideration of the cloud/aerosol coverage and profiles measured by the other elements of the EarthCARE mission [EarthCARE Mission Advisory Group, 2006].

[3] TOA flux determination requires information on the anisotropy of the radiance field emerging from the Earth-atmosphere system. If an algorithm can accurately model the

<sup>1</sup>Institute for Space Sciences, Free University of Berlin, Berlin, Germany.

<sup>2</sup>Mission Science Division, Atmospheric Section, ESTEC, European Space Agency, Noordwijk, Netherlands.

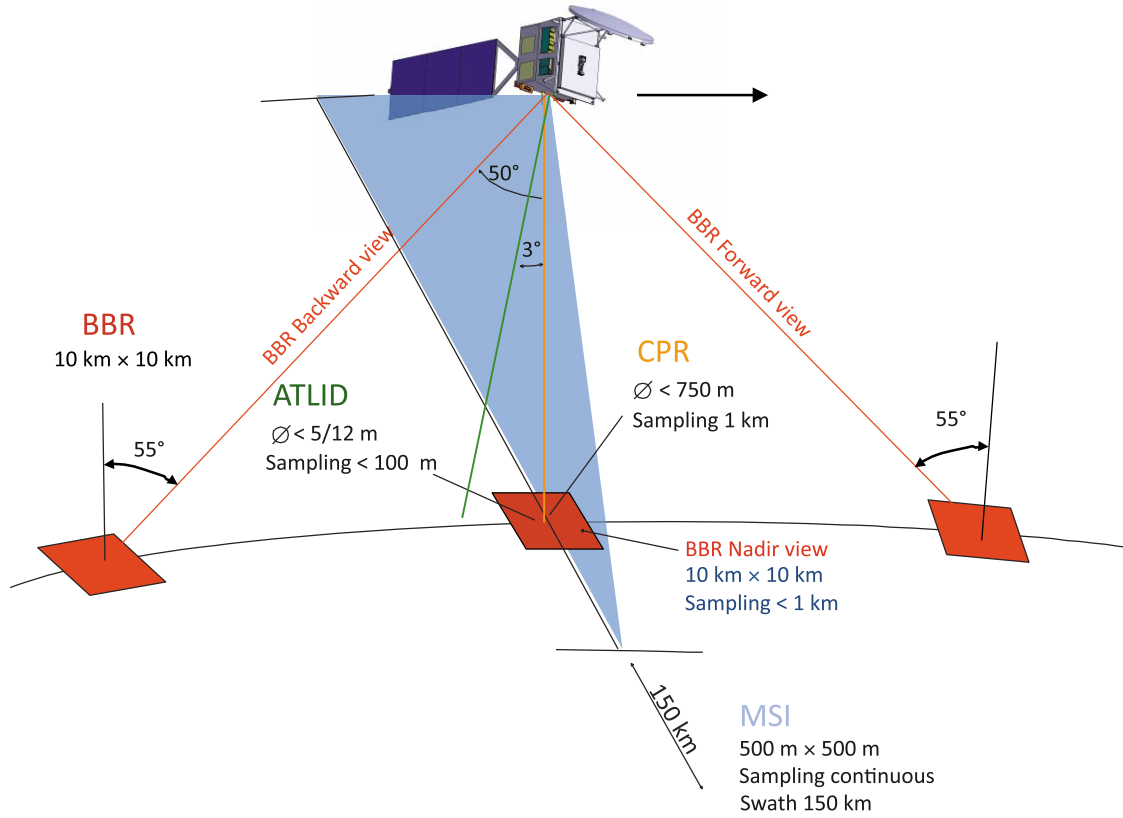


**Figure 1.** The EarthCARE satellite will carry a payload of four instruments: an atmospheric lidar (ATLID), a cloud profiling radar (CPR), a multispectral imager (MSI), and a broadband radiometer (BBR).

anisotropic distribution of the radiation field, then it could be employed to retrieve fluxes from single radiance measurements [see, e.g., *Suttles et al.*, 1988, 1989]. Flux retrieval algorithms employed in Earth radiation budget (ERB) missions such as the Earth Radiation Budget Scanning Radiometer (ScaRab) [*Kandel et al.*, 1998], the Clouds and the Earth's Radiant Energy System (CERES) [*Wielicki et al.*, 1996] and the Geostationary Earth Radiation Budget (GERB) [*Harries et al.*, 2005] use the spectral information retrieved from the target to derive TOA fluxes. The spectral information can be directly used in the flux derivation scheme as is the case with the LW GERB angular models [*Clerbaux et al.*, 2003] and the SW ScaRab-3 ADMs [*Viollier et al.*, 2009], or alternatively it can be used to describe the observed scene in the sorting into angular bins (SAB) methods employed by CERES [*Loeb et al.*, 2003, 2005]. Another possibility is to combine multiangle radiance measurements coming from the target and use theoretical or empirical bidirectional reflectance models to estimate fluxes. This approach is used with NB multiangle instruments such as Polarization and Directionality of the Earth's Reflectances (POLDER) and multiangle imaging spectroradiometer (MISR), and it was studied by *Bodas-Salcedo et al.* [2003] for a BB multiangular instrument.

[4] This study describes the angular distribution models (ADMs) employed to obtain instantaneous longwave radiative fluxes from radiance measurements of the EarthCARE

Mission. The flux retrieval algorithms developed in this work rely on a database of spectral radiance fields at TOA obtained using radiative transfer (RT) computations. The theoretical approach permits to construct conversion algorithms specifically designed for the EarthCARE instruments being able, for instance, to exploit the multidirectional and multispectral information of the BBR and MSI, or even the synergy between active and passive sensors [*Domenech et al.*, 2007]. However, the definition of theoretical angular models carries the intrinsic difficulty associated to addressing unlimited existing atmospheric conditions. In order to fairly represent the atmospheric variability, the synthetic database has been constructed on the basis of robust climatological studies and the angular models developed for the BBR measurements have been evaluated via the intercomparison against the longwave ADMs used by the CERES instrument [*Loeb et al.*, 2005, 2007] on board the Terra NASA satellite.

## 2. Methodology

[5] The radiative flux leaving the Earth-atmosphere system,  $F(\theta_0)$ , is defined as the hemispherical integration of the radiance field at TOA,  $L(\theta_0, \theta, \phi)$ , according to

$$F(\theta_0) = \int_0^{\pi/2} \int_0^{2\pi} L(\theta_0, \theta, \phi) \cos \theta \sin \theta d\theta d\phi \quad (1)$$

**Table 1.** Channel Specification of the MSI

	Wavelength Region	Center Wavelength ( $\mu\text{m}$ )
Channel 1	VIS	$0.670 \pm 0.01$
Channel 2	NIR	$0.865 \pm 0.01$
Channel 3	SWIR 1	$1.650 \pm 0.015$
Channel 4	SWIR 2	$2.210 \pm 0.015$
Channel 5	TIR 1	$8.8 \pm 0.05$
Channel 6	TIR 2	$10.8 \pm 0.05$
Channel 7	TIR 3	$12.0 \pm 0.05$

where  $\theta_0$  is the solar zenith angle,  $\theta$  the satellite viewing angle, and  $\phi$  the relative azimuth angle between the satellite and the Sun.

[6] In ERB missions, the upwelling radiance from a target on Earth at any given time is commonly measured in specific outgoing directions by narrow field of view (FOV) radiometers on board satellites; hence, the radiative flux cannot be obtained from instantaneous radiance measurements. Thus, a radiance-to-flux conversion procedure needs to be employed to estimate the exiting flux. The flux estimation can be based on an ADM model that takes the mean behavior of the anisotropy of the radiance field into account, in order to allow the flux retrieval from an observation acquired from a single viewing angle. An ADM can be defined as a lookup table of anisotropic factors,  $R$ , which are obtained as the ratio of the equivalent Lambertian flux to the actual flux:

$$R(\theta_0, \theta, \phi) = \frac{\pi L(\theta_0, \theta, \phi)}{F(\theta_0)} \quad (2)$$

[7] In this study the anisotropic factors are retrieved as a function of the BB and NB thermal radiances,  $R(\theta, \{L_{BBR}\}, \{L_{MSI}\})$ . The proposed methodology combines the operational procedure used in the LW GERB flux estimation [Clerbaux *et al.*, 2003] and previous multiangular broadband instruments studies [Bodas-Salcedo *et al.*, 2003; Domenech *et al.*, 2011]. The study is based on two main assumptions: (1) the combination of the off-nadir and nadir BBR measurements into an artificial radiance improves the flux inversion accuracy and (2) the correlation between the broadband radiances and the spectral signature of the radiation field, measured by the MSI, can be exploited to reduce the thermal flux retrieval error (see MSI spectral channels in Table 1).

## 2.1. BBR-RT Database Construction

[8] The radiative transfer computations have been performed with the LibRadtran [Mayer and Kylling, 2005] software. The BBR theoretical radiance database (BBR-RT) has been built using a molecular gas absorption parameterized with the LOWTRAN band model [Pierluissi and Peng, 1985], as adopted from the SBDART [Ricchiazzi *et al.*, 1998] code. Radiances and fluxes have been computed using the discrete ordinate solver DISORT [Stamnes *et al.*, 1988] with 16 streams for clear-sky scenes and 48 streams for cloud covers. The spectral resolution is set to  $5 \text{ cm}^{-1}$  for the thermal region from 4 to  $50 \mu\text{m}$ .

[9] A total of 9789 radiance fields have been computed for the thermal region of the solar spectrum for the three BBR viewing angles simulating realistic conditions of the

Earth-atmosphere system. The study assumes that the dependence of the LW anisotropy on  $\phi$  is negligible in most conditions [Loeb *et al.*, 2003, 2005]. Although this assumption should be revised in further studies, in particular for clear regions consisting of rough terrain where the LW anisotropy is shown to depend systematically on the azimuth angle [Minnis and Khaiyer, 2000].

[10] The model inputs have been randomly selected in the variation intervals in order to avoid, as far as possible, the introduction of biases in the database. Depending on the parameter under consideration, two sampling methods have been employed: pseudorandom numbers for which different seeds lead to unique computation; and quasi-random numbers, which appear more uniform, avoiding clumping.

### 2.1.1. Clear-Sky Scenes

[11] For each scene in the synthetic database, the parameters to consider in clear sky are the following.

#### 2.1.1.1. Atmospheric Conditions

[12] The aerosol model and loading in the boundary layer are set randomly and with equal probability within rural, maritime, urban and tropospheric types [Berk *et al.*, 1998]. Background aerosols are selected above 2 km. The aerosol profile (spring-summer or fall-winter) is specified according to the atmospheric profile date. These climatological profiles are obtained from the Thermodynamic Initial Guess Retrieval (TIGR) databases [Chevallier *et al.*, 1998, 2000]. The profiles in the TIGR2000\_v1.1 have been extended up to the TOA level according to the corresponding standard atmospheres [Anderson *et al.*, 1986] and extra gas species (air density,  $\text{O}_2$ ,  $\text{CO}_2$  and  $\text{NO}_2$ ) were added. A uniform random permutation is performed over the 2300 TIGR profiles to include the radiosonde information in the model inputs. The atmospheric profile selected provides the geographic location of the input to be employed in the clouds statistics.

#### 2.1.1.2. Surface Emissivity and Temperature

[13] The emissivity is dependent on the wavelength and is selected from the International Geosphere and Biosphere Program (IGBP) albedo library [Wilber *et al.*, 1999] that corresponds to the radiosounding location selected by the input. The skin temperature is randomly chosen close to the lowest atmospheric profile level according to the illumination conditions (daytime/nighttime).

### 2.1.2. Cloudy Scenes

[14] The clouds have the highest influence in the anisotropy of the radiance field. Therefore, it is of paramount importance to include realistic statistics in the cloud modeling. A climatological analysis based on Cloud-Aerosol Lidar and Infrared Pathfinder Satellite Observation (CALIPSO) and CERES Terra data has been performed to obtain a probability density function (PDF) of cloud phase, cloud altitude and cloud fraction parameters for the different latitudinal bands.

[15] A number of 50 orbits of CALIPSO vertical feature mask product (v2.01) corresponding to January 2007 (randomly chosen with no distinction for day/night orbits) have been processed in the analysis. Figure 2 shows the cloud statistics of ice and water clouds for the latitudinal intervals defined by the standard atmospheres. Considering these results, ice/water clouds are classified by their cloud top height (CTH) as low, middle or high clouds. The number of levels and their altitude range are defined as a

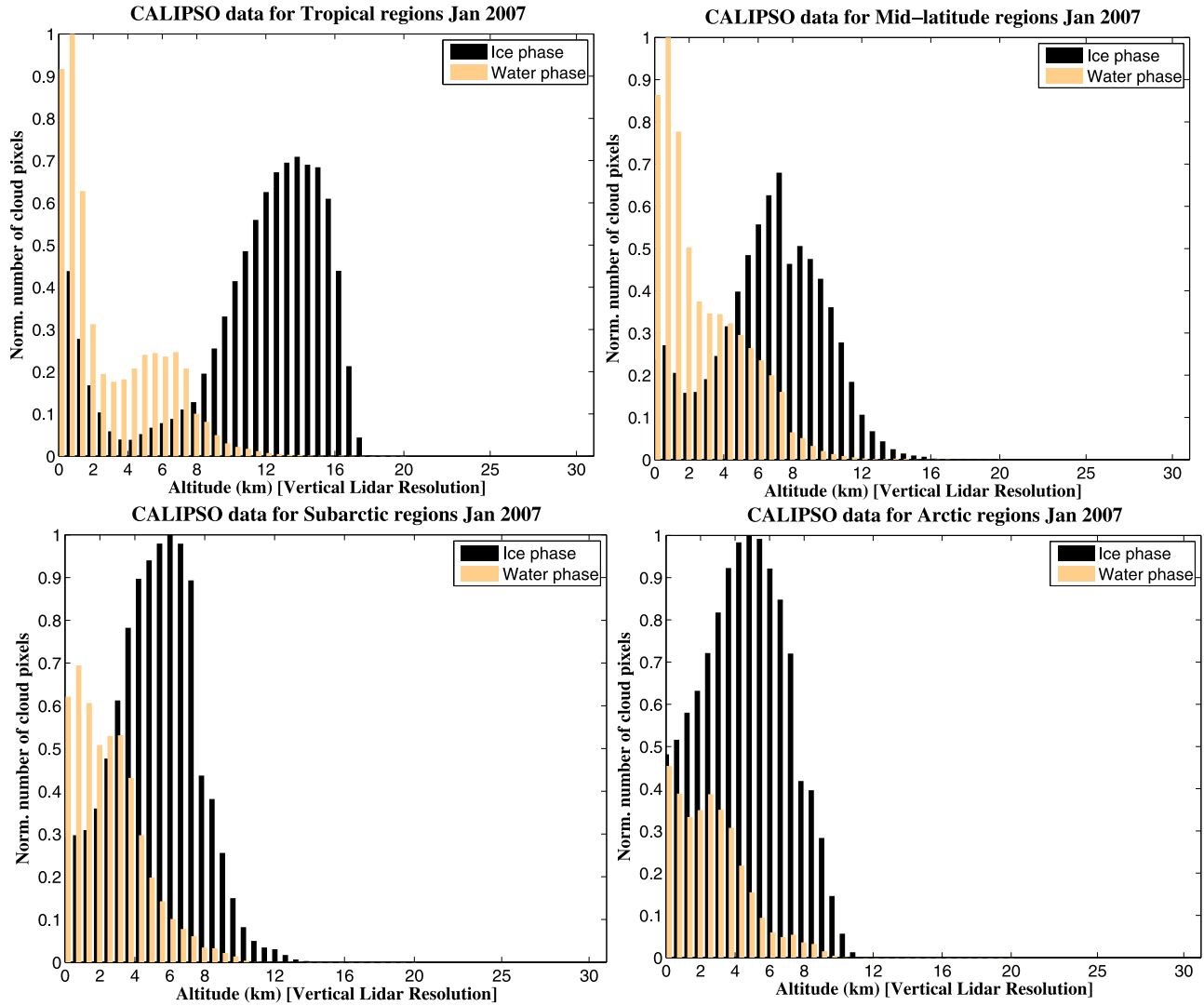


**Figure 2.** Statistics of cloud parameters sorted by the latitudinal bands obtained from 1 month of CALIPSO vertical feature mask product.

function of the latitude for both ice and water clouds. The PDF of the cloud altitude intervals for each latitudinal region provides the likelihood to find water or ice phase clouds in the radiance database. Thus, the cloud statistics obtained from CALIPSO data are fitted to the generalized extreme value (GEV) distribution function, so that the cloud altitude and thickness parameters to be included in the simulations can be randomly chosen. Figure 3 shows the probability density functions employed in the ice and water clouds between the tropics and the polar regions.

[16] The multilayer probability used in the input creation (60% single layer, 30% double layer, 10% as three or more layers) is based on that of Wang *et al.* [2000]. However, only single and double cloud layers are considered in this paper. Cloud optical thickness (COT) is selected within the limits used in the CERES Terra ADMs according to the cloud thickness and the CTH. The cloud cover is chosen on the basis of the statistics obtained from 8 days of CERES along-track data (see section 3.1 for more details). The results are shown in the Figure 4. The ice water content and effective particle radius are translated to optical properties

with parametrizations similar to Key *et al.* [2002], and the water properties are obtained using precalculated Mie tables. The microphysical properties for ice clouds are randomly selected among five ice crystal habits [Yang *et al.*, 2000] available in the RT code.

### 2.1.3. Verification

[17] The modeled radiance fields have been compared to NB advanced very high resolution radiometer (AVHRR) and BB CERES radiances in order to assess the goodness of the RT simulations. The AVHRR and CERES instruments were selected because they present similar characteristics to the proposed EarthCARE analogous sensors. However, the MSI channel  $8.8 \mu\text{m}$  is not available in AVHRR. Five AVHRR MetOp-A orbits have been employed in the study. The modeled NB radiances were convolved with the AVHRR spectral response function (SRF) and compared with the actual data. Figure 5 (top) shows the scatterplot of the radiances at  $10.8$  against  $12.0 \mu\text{m}$  for the modeled data and one orbit of AVHRR observations. Although the plot shows a good correlation, the ratio between TIR  $12.0$  and TIR  $10.8$  is slightly higher in simulation than in observations. In

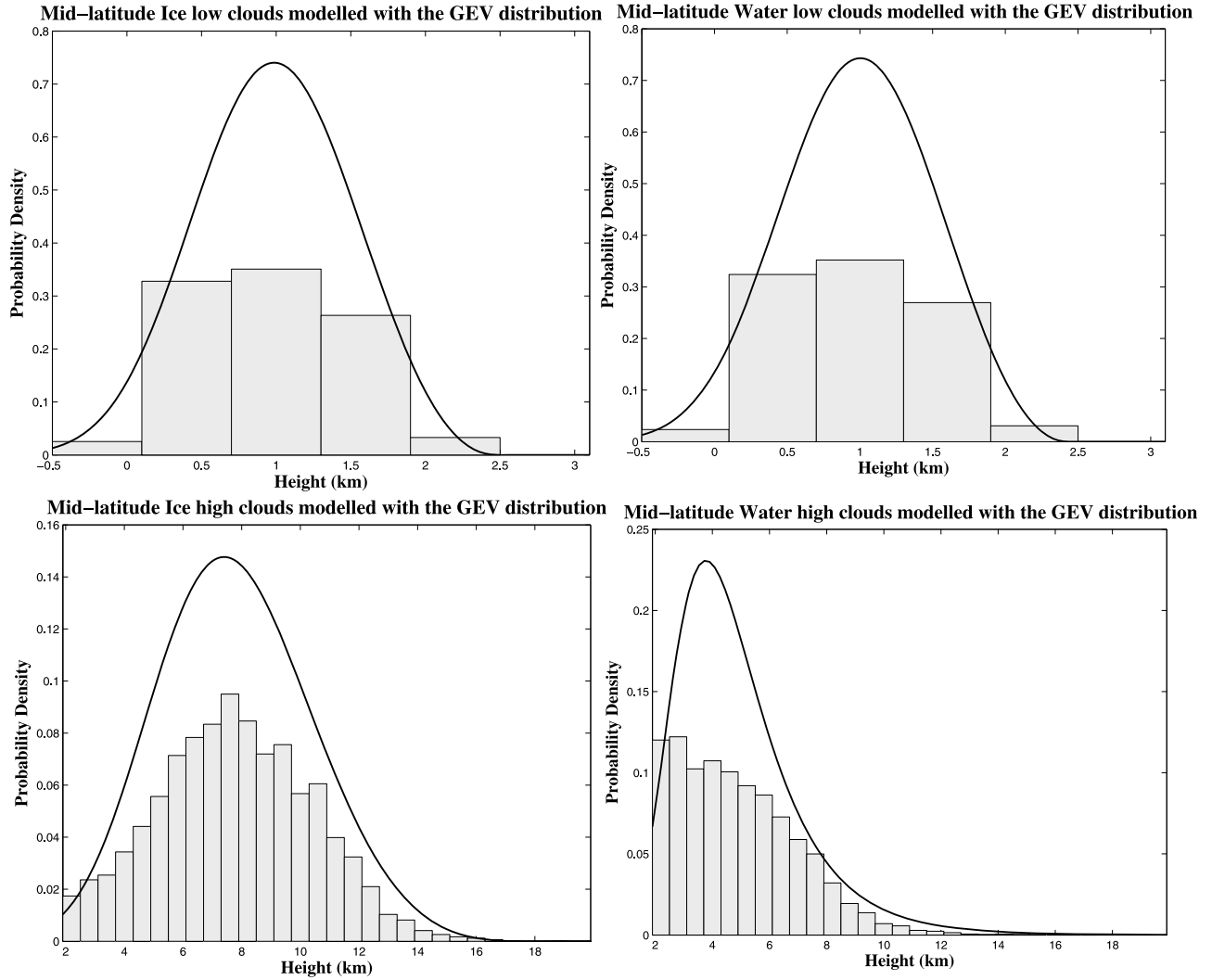


**Figure 3.** Example of the GEV fitting obtained for midlatitude clouds. Grey bars correspond to the scaled histograms of Figure 2. The overlaid black lines are the PDFs for the fitted GEV models. The histograms are scaled so that the bar heights times their width sum to 1 to make them comparable to the PDF.

particular, for warm and hot scenes. The remaining four orbits analyzed show a similar pattern. The frequency distribution of AVHRR/libRadtran 10.8 and 12.0  $\mu\text{m}$  radiances is shown in Figures 5 (middle) and 5 (bottom), respectively. Figure 5 (middle and bottom) points out the coherence of the results; however, it seems to be an underestimation of hot surfaces in the radiance database.

[18] The CERES AT database employed to evaluate the BBR ADMs (see section 3.1) is used here to verify the correct distribution of the modeled BB thermal radiances. The CERES/modelled radiance ratio is computed following the approach shown by Clerbaux *et al.* [2009]. The CERES and model radiances are binned independently according to the viewing angle and cloud conditions in bins of  $10 \text{ W m}^{-2} \text{ sr}^{-1}$ . Then the radiances are averaged and the ratio performed. Figure 6 does not show significant differences for nadir and off-nadir views. The distribution of modeled radiances agrees quite well with the CERES data set, except for cold clear-sky scenes where the simulations slightly overestimate the radiances.

## 2.2. LW BBR-ADMs Development

[19] The BBR-RT database is used to both develop and assess the BBR angular models. While one half (randomly selected) of the database is used to fit the models on the data, the second half is employed in the error analysis. In the methods discussed in sections 2.2.1–2.2.5, the model is fitted on the BBR-RT database to invert the anisotropic coefficient from the theoretical radiances,  $L(\theta)$ , and flux,  $F$ , according to equation (2). Since the viewing geometry of the BBR fixes the observations at nadir and 50 degrees, only those angles are considered to build the models. Once the anisotropic factors are retrieved, the estimated BBR LW fluxes are computed for the evaluation of the theoretical models. In this step, the root mean square errors (RMSE) between modeled and derived fluxes are calculated.

[20] Table 2 lists the angular models developed for the BBR and the measurements needed to successfully apply the radiance-to-flux conversion algorithms. The theoretical accuracy obtained for every model and analyzed in sections 2.2.1–2.2.5 is also summarized in Table 2.

Cloudiness distribution for 8 days of CERES Terra true along-track data

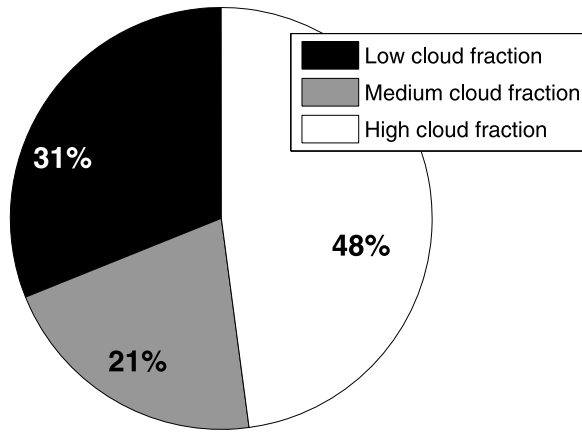


**Figure 4.** Cloud cover distribution for 8 days of true along-track CERES data.

### 2.2.1. Single-View Nonspectral ADM Model

[21] The simplest algorithm to evaluate fluxes from radiances corresponds to the single-view and nonspectral models. Considering that the inversion error inferred from these models will be a priori the highest, these results will be used as reference for the evaluation of the following discussed models. In these ADMs, the anisotropic factor is expressed by

$$R(\theta, L) = c_0(\theta) + c_1(\theta)L(\theta) \quad (3)$$

where  $c_0(\theta)$  and  $c_1(\theta)$  are the corresponding linear regression coefficients for each observation angle ( $0^\circ$  and  $50^\circ$ ).

[22] Figure 7 shows the performance when this approach is employed for the BBR views. The theoretical  $R$  is compared to the  $R$  predicted by the angular model for every scene. The results do not show large differences in the TOA flux retrievals because of the smooth anisotropic nature of LW radiance field. The lowest error is associated with the observation at  $50^\circ$  because of the low dependence on the scene type and the reduced anisotropic effect around this angle [Bodas-Salcedo et al., 2003; Otterman et al., 1997]. On the other hand, as expected the worst inversion is obtained for the nadir view. On average,  $R$  increases linearly with the radiance [Bodas-Salcedo et al., 2003; Clerbaux et al., 2003], and hence the anisotropy could be roughly characterized by a linear model. However, this model does not account for the strong anisotropy of cirrus clouds corresponding to the scattered points of Figure 7 (bottom).

### 2.2.2. Multiangular Nonspectral ADM Model

[23] The along-track views of the EarthCARE BBR enable to measure three radiances coming from the same source at almost the same time. This configuration provides an angular information on the radiance field anisotropy that can be employed to improve the single-view based ADMs. The ADM definition can be extended to use the three views in the flux estimation. By defining a new magnitude, an effective radiance, equation (2) takes the form

$$R = \frac{\pi I}{F} \quad (4)$$

where  $I$  is the so-called effective radiance. The effective radiance can be expressed in different ways [Bodas-Salcedo et al., 2003]. In this study, the effective radiance is obtained from the line integral limb to limb over  $\theta$ :

$$I = \int_{-\frac{\pi}{2}}^{\frac{\pi}{2}} \check{L}(\theta) |\sin \theta| \cos \theta d\theta \quad (5)$$

where  $\check{L}(\theta)$  is the second degree polynomial fit of the three along-track radiances  $\{L_{BB}\}$  as a function of  $\theta$ :

$$\check{L}(\theta) = \sum_{n=0}^2 a_n(\theta) \theta^n = a_0 + a_1 \theta + a_2 \theta^2 \quad (6)$$

with  $a_n$  being the fitting parameters and  $\theta$  the independent variable.

[24] If the anisotropic factor is simply estimated from  $R(I) = c_0 + c_1 I$  (Figure 8), the radiance-to-flux conversion error is reduced by 88% and 14% compared to the results obtained with the nadir and off-nadir single-view non-spectral methods, respectively.

### 2.2.3. Single-View Multispectral ADM Model

[25] This section estimates the flux inversion improvement when the spectral signature,  $L(\lambda)$ , of the scene is available. The thermal bands of the MSI instrument,  $\{L_{NB}\}$ , namely at 8.8, 10.8 and 12.0  $\mu\text{m}$ , together with the individual BB radiances,  $L_{BB}(\theta)$ , are used to calculate the anisotropic coefficients. Following the approach of Clerbaux et al. [2003],  $R(\theta)$  is estimated as a third-order regression on the BBR BB radiance and MSI NB radiances without particular physical meaning for the regression coefficients. A direct use of the three thermal MSI measurements in high-order regressions produces lot of coefficients (35 coefficients for second order, 70 coefficients for third order, etc.), thus a principal component analysis (PCA) is recommended to limit the number of parameters. (It is commonplace for the sum of the variances of the first few PCs to exceed 80% of the total variance of the original data.) The spectral information is projected on the principal component axis (linear transformation) and the angular models are constructed on a restricted set of the principal components.

[26] Figure 9 shows how the model using the nadir or the oblique BBR view reproduces the anisotropic behavior of the modeled radiance fields. The use of the MSI spectral data allows to reduce the conversion error by about 41% in the worst case (nadir). According to Clerbaux et al. [2003] results, the exploitation of the spectral signature from multichannel imagers like the Moderate Resolution Imaging Spectroradiometer (MODIS) allows a reduction of the radiance-to-flux conversion error of about 45%. The better performance of this model when it is adapted to the MODIS configuration is due to the higher number of available channels in the thermal part of the spectrum.

### 2.2.4. Single-View Monospectral ADM Model

[27] The radiance-to-flux conversion using information from a single NB radiance is of interest since the daytime data employed in the model evaluation have only one NB thermal MODIS channel (MODIS channel 31 = 11.03  $\mu\text{m}$ ) with coincident BB CERES observations.

[28] This angular model is a simplified version of the former single-view multispectral model. In particular, this

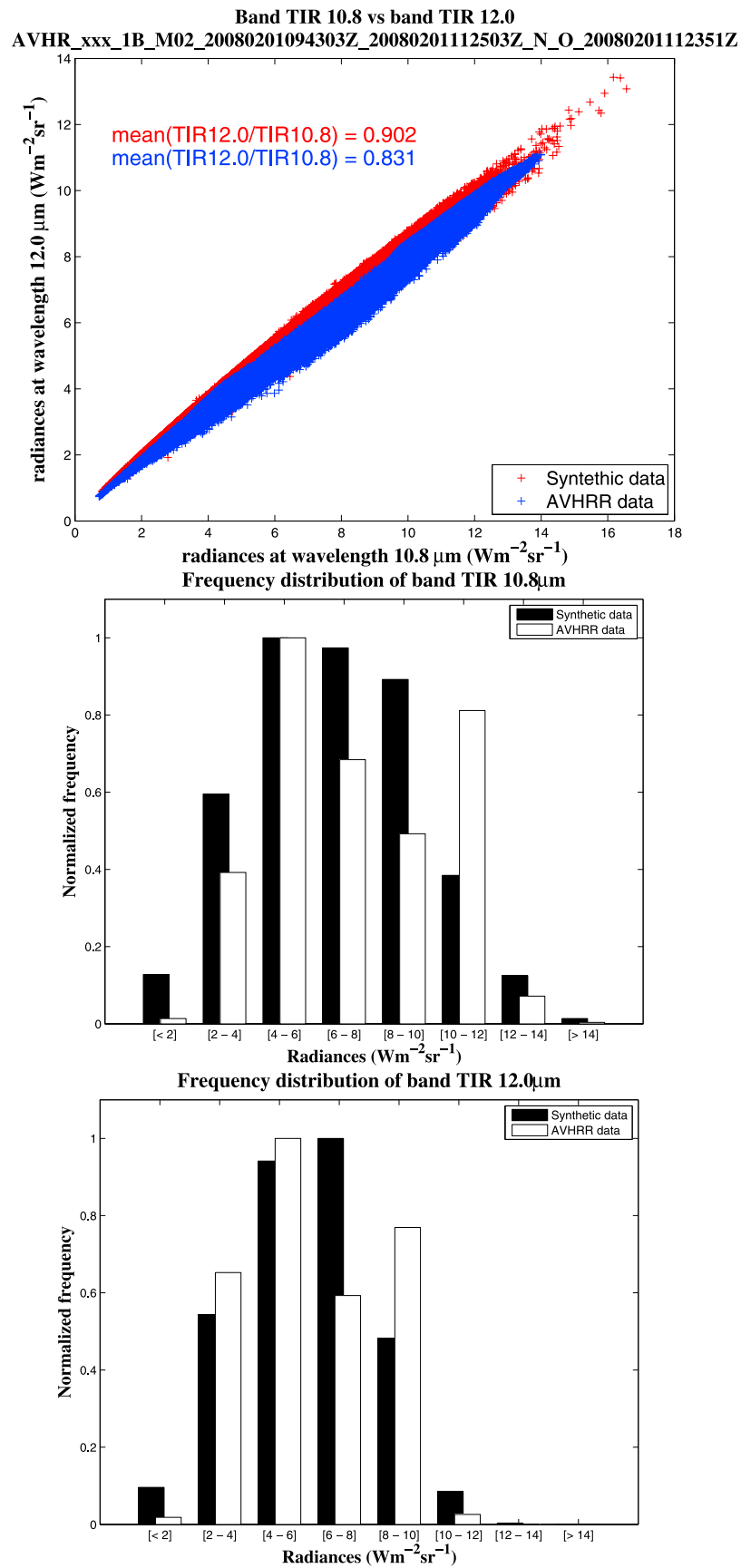


**Figure 5.** Comparison of NB modeled data against observed AVHRR NB radiances.

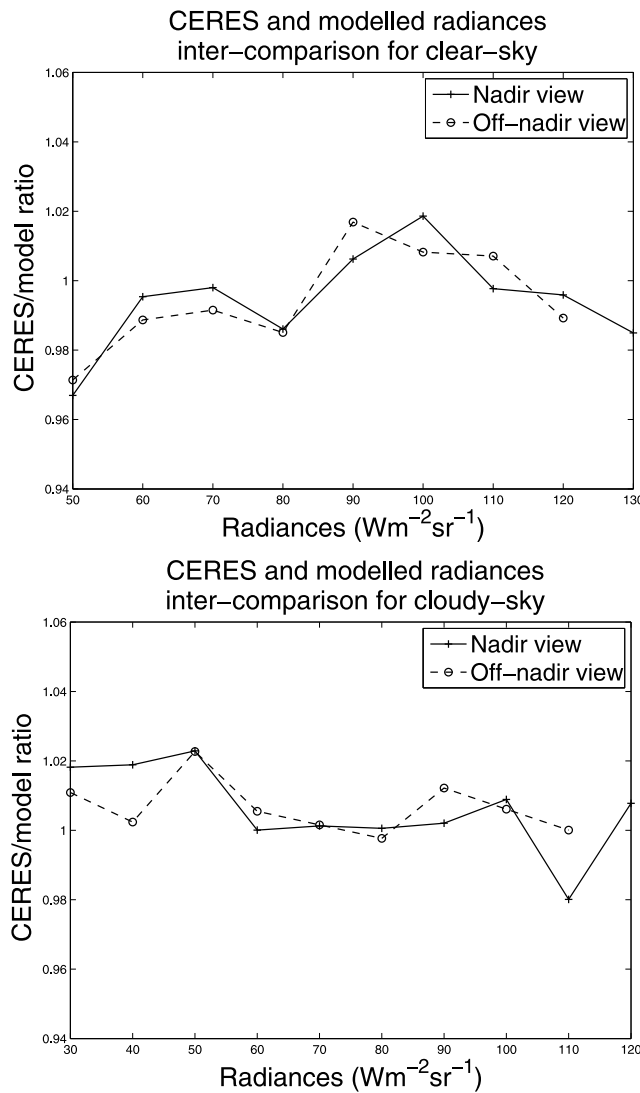


**Figure 6.** Evaluation of BB LW modeled radiances compared to LW CERES measurements.

ADM uses a general nonlinear regression (third order) in which the theoretical anisotropic factors (computed from equation (2)) are modeled by a function which is a nonlinear combination of the BBR BB and MSI NB (channel 6) radiances simulated per each scene. The performance of this model is displayed in Figure 10. These ADMs improve the results achieved with the single-view nonspectral model; however, the error reduction is much less than the diminu-

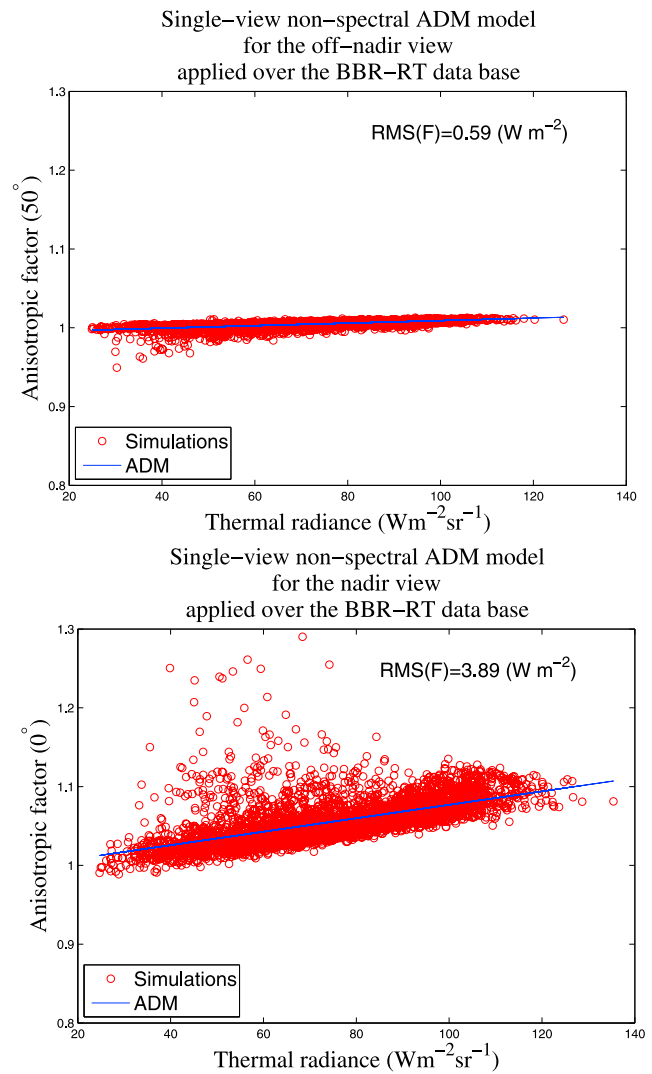


**Figure 7.** Comparison of anisotropic factors theoretically retrieved for each scene against anisotropic factors obtained with the single-view nonspectral ADM at the BBR viewing angles.

tion obtained with multiangular or multispectral ADM models.

### 2.2.5. Multiangular-Spectral ADM Model

[29] Sections 2.2.1–2.2.4 outlined that the along-track effective radiance captures more angular information of the target than using a single view. Furthermore, the correlation between the spectral signature and the anisotropy behavior

**Table 2.** Summary of LW BBR Angular Models<sup>a</sup>

BBR LW ADMs	RMSE Flux ( $\text{W m}^{-2}$ )	Requirements
Single-view nonspectral nadir model	3.89	BBR radiance at nadir
Single-view nonspectral oblique model	0.59	BBR radiance at $50^\circ$
Multiangular nonspectral model	0.51	Oblique + nadir BBR radiances
Single-view multispectral nadir model	2.29	Nadir BBR + thermal MSI radiances
Single-view multispectral oblique model	0.44	Oblique BBR + thermal MSI radiances
Single-view monospectral nadir model	3.47	Nadir BBR + MSI band 6 radiances
Single-view monospectral oblique model	0.54	Oblique BBR + MSI band 6 radiances
Multiangular/spectral model	0.40	3 BBR + thermal MSI radiances

<sup>a</sup>The measurements required to use the ADMs and the theoretical performance for every model are listed.



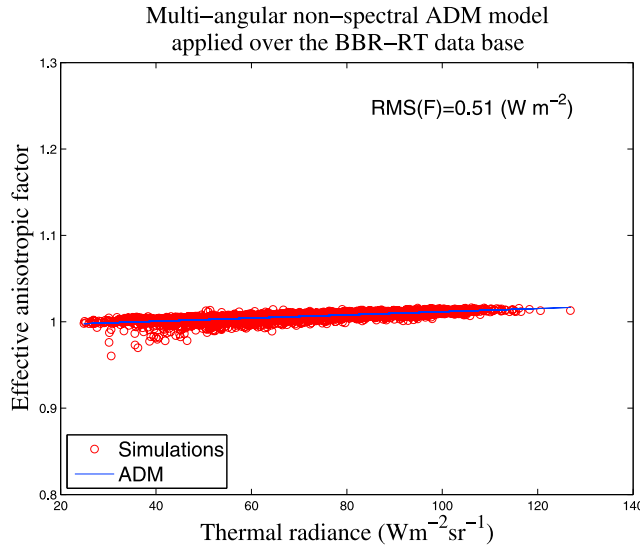


**Figure 8.** Scatterplot of anisotropic factors,  $R(\theta)$ , retrieved from the simulations and from the multiangular nonspectral model against thermal effective radiances,  $I(\theta)$ .

has also been successfully addressed. This section combines both approaches to improve the BBR flux conversion. A third-order regression using the BBR BB effective radiance and the first two terms of the PCA on the MSI radiances is employed, and the  $R(\{L_{BB}\}, \{L_{NB}\})$  takes the form as follows:

$$\begin{aligned}
 R(I, L_{PCA1}, L_{PCA2}) = & a_0 + a_1 L_{PCA1} + a_2 L_{PCA2} + a_3 I + a_4 L_{PCA1}^2 \\
 & + a_5 L_{PCA2}^2 + a_6 I^2 + a_7 I L_{PCA1} + a_8 L_{PCA2} I \\
 & + a_9 L_{PCA1} L_{PCA2} + a_{10} L_{PCA1}^3 + a_{11} L_{PCA2}^3 \\
 & + a_{12} I^3 + a_{13} L_{PCA1} L_{PCA2} I + a_{14} L_{PCA1}^2 L_{PCA2} \\
 & + a_{15} L_{PCA1} L_{PCA2}^2 + a_{16} L_{PCA1}^2 I + a_{17} L_{PCA1} I^2 \\
 & + a_{18} L_{PCA2}^2 I + a_{19} L_{PCA2} I^2
 \end{aligned} \quad (7)$$

[30] The analysis of errors (Figure 11) shows that the model fits the data very accurately with some minor problems for cold scenes. This method allows a reduction of the radiance-to-flux conversion error up to 82%, 10% and 18% with respect to the nadir multispectral, off-nadir multispectral and multiangular models, respectively.

### 3. Results: Evaluation Using CERES Along-Track Data

[31] The multiangular/spectral model seems to be very promising according to the results reached in the theoretical error analysis. However, it is difficult to extrapolate the algorithms obtained from simulated data to satellite measurements. Mainly, because the sampling in the database construction is certainly biased. Consequently they should be validated by means of satellite-based data as well.

#### 3.1. BBR-like Database Creation From CERES Measurements

[32] The radiance measurements to be employed in the evaluation of the BBR algorithms have to reproduce the

forthcoming BBR observations. An instrument able to measure three BB LW radiances of the same scene at nadir and oblique  $50^\circ$  is required. Additionally, coincident NB radiances in the thermal region of the spectrum are also requested in order to apply the methodology.

[33] The ERB missions with both BB and NB instruments on board the same platform are limited. Nevertheless, the payload of the NASA satellite Terra fulfils the requirements, with the CERES and the MODIS instruments aboard. The AT Terra CERES-MODIS single-scanner footprint (SSF) data sets are perfectly suited for the study. This product integrates coincident measurements from MODIS and CERES flying model instruments FM1 and FM2. However, not all the AT observations are useful for this assessment study. Only those obtained after the Earth rotation correction applied over the AT scanning mode [Capderou and Viollier, 2006] are valid (February 2005), otherwise the colocation between the nadir and oblique views is only possible at the highest latitudes when the orbit turns back and the satellite

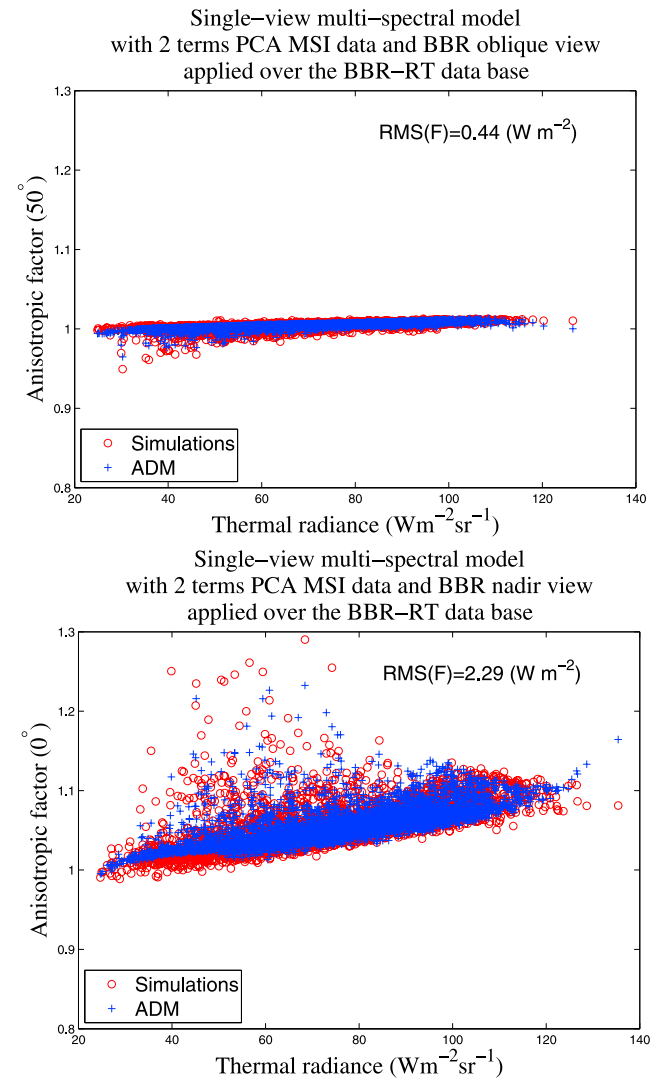


**Figure 9.** Comparison of anisotropic factors theoretically retrieved for each scene against anisotropic factors obtained with the third-order regression of the multispectral model using two PCA terms of MSI data and BBR observations.

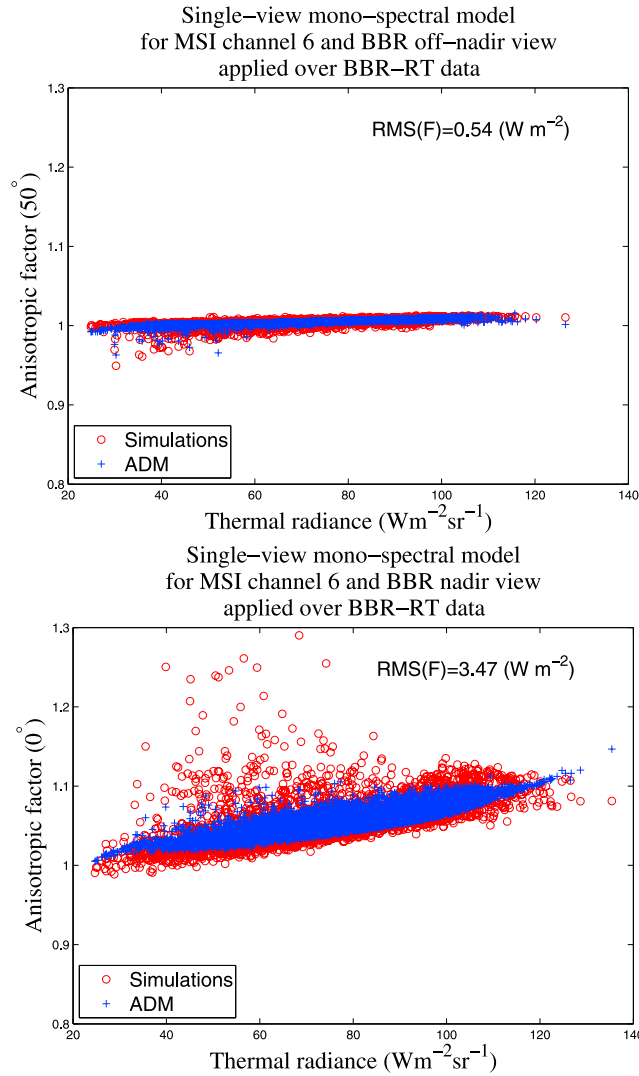


**Figure 10.** Scatterplot of anisotropic factors,  $R(\theta)$ , obtained from the simulations and from the monospectral model using the MSI channel at  $11.0 \mu\text{m}$  against thermal radiances. Plots shown for the nadir and oblique BBR observations.

follows the Earth rotation. The FM2 CERES instrument switched to AT operation mode during daytime every 15 days. In nighttime returned to cross-track azimuth mode. However, different issues concerning the early ageing of the sensor recommended to restrict the AT scanning mode of the CERES sensors. Therefore, CERES true along-track (TAT) radiances are not currently being scanned and all the available CERES TAT data collected in the Atmospheric Science Data Center (ASDC) are used in this study. In particular, 8 days of CERES data have been used, 2 days for January 2005: 11, 25 (noncorrected AT scanning mode) and 6 days for February 2005: 8, 22, 25, 26, 27, 28 (TAT scanning mode). The noncorrected AT orbits have been employed to enlarge the database with nighttime measurements. Nevertheless, the scene sampling of those observations only contains clear and cloudy snow/ice footprints.

[34] A subset of CERES AT data (hereafter CERES-BBR-like data) is used to test the angular models described

in section 2.2. The LW BBR flux retrieval algorithms are not azimuthally dependent. Thus, the criteria for constructing the CERES-BBR-like database consist in selecting CERES footprints temporally and spatially colocated in nadir and in any of the  $50^\circ$  oblique views. The angle interval allowed for the oblique and nadir angles ranges between  $45^\circ$  and  $55^\circ$  and  $0^\circ$  and  $5^\circ$ , respectively. The distance between nadir and oblique CERES field-of-view (FOV) centers selected is less than 10 km. In addition, several filters have been applied to verify the flux consistency for nadir and off-nadir targets. Namely, the selection is performed firstly when the ADM identifier (ID), the cloud classification parameter (CCP) (used by CERES to define the cloud type and number layers present in the scene) and the MODIS bands employed in the scene identification in the nadir and off-nadir CERES FOVs match and secondly when the difference between MODIS radiance measurements over nadir and oblique CERES FOVs is less than 15%. These criteria are selected to improve the coherence of the CERES-BBR-like database but on the other hand reduce significantly the statistics. The BBR algorithms are evaluated against CERES flux estimates, thus CERES fluxes with discrepancies between nadir and off-nadir views (ideally equal) higher than the 5% of the maximum flux estimated for the target are discarded (13.2% of the population).

[35] The CERES-BBR-like database should include the radiance information corresponding to the MSI thermal bands. The point spread function (PSF) weighted mean of the radiances associated with all MODIS pixels convolved in the CERES FOV is included in the SSF data sets. The nearest MODIS NB channels to those implemented in the MSI are centered at  $8.55$ ,  $11.03$  and  $12.02 \mu\text{m}$  which are, in fact, a good approximation. Unfortunately, the imager channels recorded in the SSF data files vary between footprints (see Table 3). In particular, the three required bands are only available in nighttime. Thus, only clear/cloudy snow surfaces are included in the CERES-BBR-like data

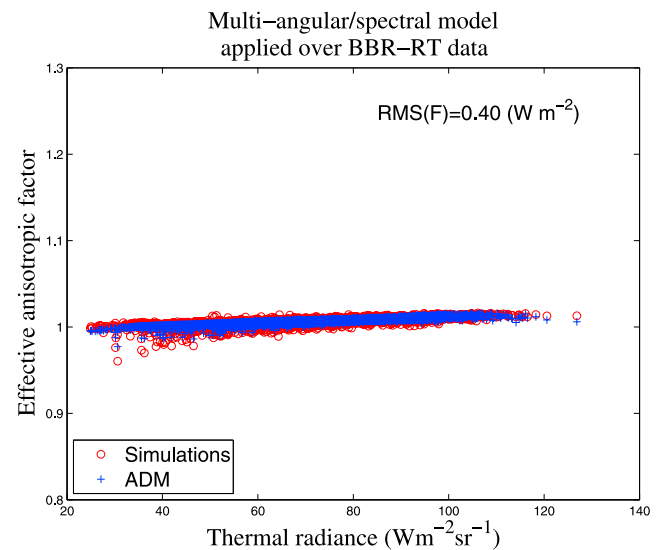


**Figure 11.** Comparison of anisotropic factors theoretically retrieved for each scene against anisotropic factors obtained with the multiangular or spectral ADM model.

**Table 3.** MODIS Channels Selected in the CERES Terra SSF<sup>a</sup>

Index	Day, Solar Zenith <90	Night, Solar Zenith >90
1	0.64 $\mu\text{m}$	8.5 $\mu\text{m}$
2	0.47 $\mu\text{m}$ (odd) 1.6 $\mu\text{m}$ (even)	13.3 $\mu\text{m}$
3	3.7 $\mu\text{m}$	3.7 $\mu\text{m}$
4	11.0 $\mu\text{m}$	11.0 $\mu\text{m}$
5	0.86 $\mu\text{m}$	12.0 $\mu\text{m}$

<sup>a</sup>Odd refers to odd days in the calendar month, and even refers to even days within the calendar month.

with three thermal NB radiances. The CERES observations acquired in daytime only contains the MODIS band 31 corresponding to 11.03  $\mu\text{m}$ .

### 3.2. Construction of CERES ADMs for Use With CERES TAT Observations

[36] Since CERES and MODIS instrument technical specifications are different from BBR and MSI, specific angular models (CERES-BBR-ADMs) have been built in order to perform the comparison between flux retrievals over the CERES-BBR-like measurements. A synthetic database of CERES and MODIS radiances (CERES-RT) has been constructed from the BBR-RT data set. The NB MODIS integrated radiances are obtained considering MODIS band 29 (band center 8.5288  $\mu\text{m}$ ; band width 369.2 nm), MODIS band 31 (band center 11.0186  $\mu\text{m}$ ; band width 510.3 nm), and MODIS band 32 (band center 12.0325  $\mu\text{m}$ ; band width 493.5 nm) and filtered by the corresponding MODIS relative spectral responses.

[37] The CERES-BBR-ADMs have been obtained following the procedure shown in section 2.2. As in the case of the LW BBR-ADMs, one half of the database has been used to build the models and the other half to evaluate them. As expected, the error analysis performed shows similar results to those obtained in the LW BBR-ADMs.

### 3.3. Model Evaluation

[38] The CERES-BBR-ADMs developed on the basis of the BBR-ADMs are evaluated in this section using the CERES-BBR-like data set. The fluxes derived from these models are compared to the CERES Terra flux estimates [Loeb *et al.*, 2005] delivered for every scene. The analysis is performed over scene subsets sorted by the CERES LW ADM ID (scene type). Namely, six scene types: clouds over water, clouds over land/desert, clear snow and cloudy, clear water, clear land/desert and clear mixed surface type.

[39] RMSE and mean absolute error (MAE) metrics have been computed for all the fluxes retrieved from the CERES Terra and CERES-BBR ADMs in the CERES-BBR-like data set. The normalized mean error (NME) and the mean bias are obtained for every subset of scenes sorted by the LW ADM ID. The NME metric is a relative difference normalized by observations (CERES Terra flux estimates in this case), described by

$$NME = \frac{\sum |F_{BBR} - \bar{F}_{CERES}|}{\sum \bar{F}_{CERES}} \quad (8)$$

where  $F_{BBR}$  is the flux derived from the CERES-BBR-ADMs and  $\bar{F}_{CERES}$  is the flux estimated by the CERES

Terra ADMs (corresponding to the average between nadir and oblique retrieved fluxes). The NME assumes that CERES Terra flux estimates are the absolute truth and it is biased for small numbers in the denominator. However, this metric typically gives a better sense of the model performance compared to other metrics and do not require an observation-based minimum threshold [Boylana and Russell, 2006]. These metrics are shown in Figures 12 and 13 together with the correlation coefficient (denoted by R in the plots).

[40] Two different analysis have been performed taking into account the different availability of MODIS channels in the CERES-BBR-like database. In particular, an all-sky study considering all the scenes with coincident CERES and MODIS band 31 observations (corresponding to more than 1,500,000 targets) and another analysis employing more than 80,000 scenes with coincident CERES and MODIS bands 29, 31 and 32 data. However, the latter study is limited and biased because the three thermal channels are mainly present over clear and cloudy snow surfaces. Table 4 shows the number of targets corresponding to these analyses.

[41] It is necessary to take into account some considerations in order to understand the results of the model evaluation. CERES Terra flux estimates are used as reference in this study. However, CERES instantaneous flux accuracy is shown to be slightly dependent on the scene with uncertainties up to 2.3% for fluxes obtained in midlatitude regions (see Table 5). Additionally, some discrepancies can be found in the CERES flux estimates over the same target because of the different spatial resolution between nadir and oblique CERES views. This issue was considered in the CERES-BBR-like database creation (see section 3.1), although significant uncertainties can still be present. Table 6 shows the averaged differences between fluxes obtained from nadir and off-nadir CERES observations, these discrepancies should be considered the maximum error associated to the CERES fluxes for each of the subsets.

### 3.4. Empirical Evaluation of CERES-BBR-ADMs Using CERES TAT and MODIS Channel 31

[42] Figure 12 shows the performance of the CERES-BBR-ADMs applied over CERES footprints under all-sky conditions. As expected, the nadir view nonspectral angular model (Figure 12, top), which is the simplest method with the worst angle acquisition in terms of ADM inversion, shows the largest discrepancies (RMS errors up to 4.6  $\text{W m}^{-2}$ ). In general, CERES-BBR-ADMs underestimate the CERES flux retrievals being particularly significant the bias in clear water scenes (5.2  $\text{W m}^{-2}$ ). The oblique view nonspectral angular model shows much better results. The viewing angle at 50° is optimum for the flux inversion [Stubenrauch *et al.*, 1993; Bodas-Salcedo *et al.*, 2003] and this is clearly shown in Figure 12 (top right). The results are notably good for clear-sky water and land surfaces. Also, the large reduction in the uncertainty with respect to the nadir view (38%) is remarkable.

[43] According to the theoretical error analysis, the availability of additional angular or spectral information in the radiance-to-flux conversion increases the retrieved flux accuracy. The multiangular nonspectral model confirms the results previously obtained (Figure 12, middle left). The use of the effective radiance in the thermal flux retrieval algo-

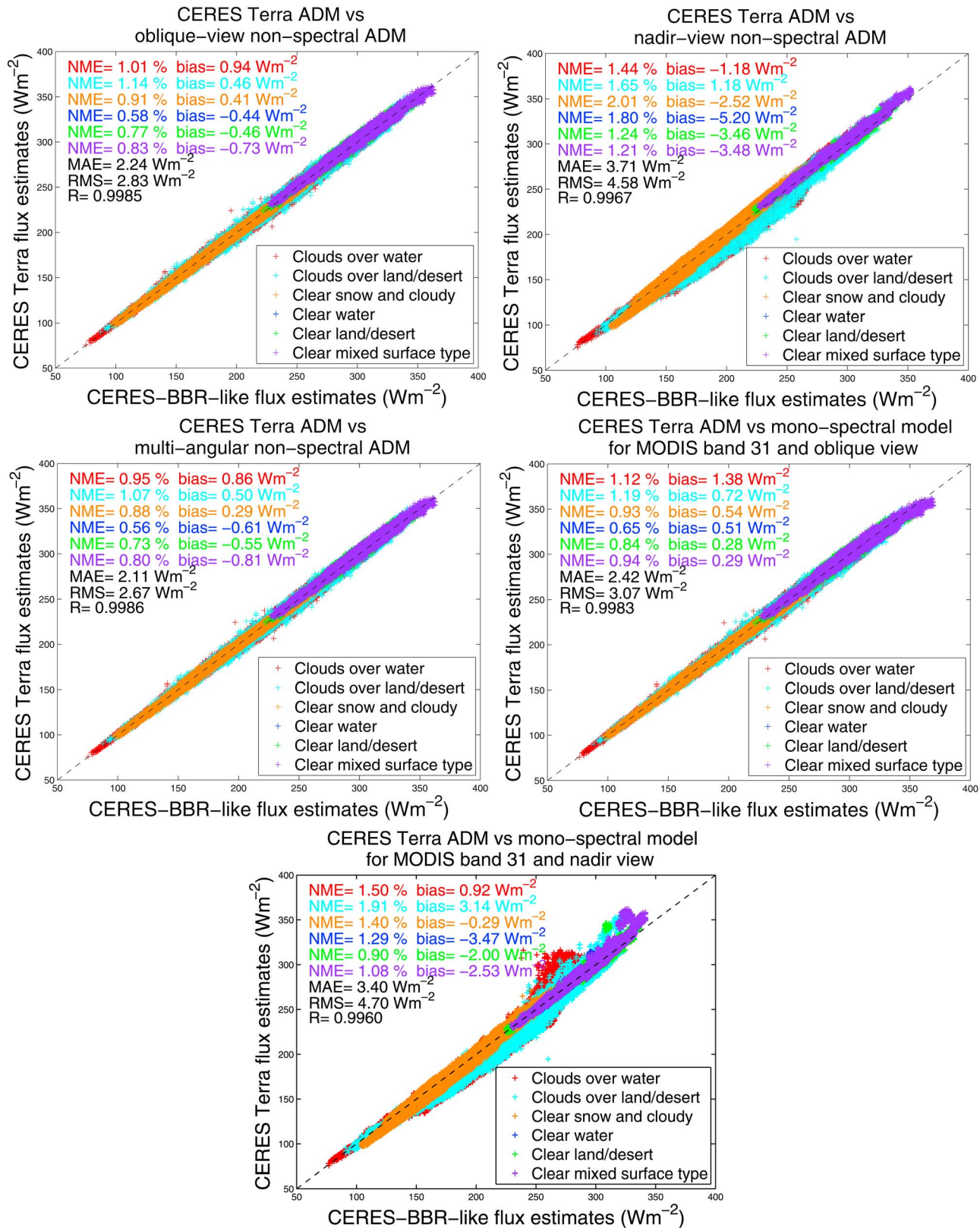


**Figure 12.** Evaluation of TOA fluxes estimated from LW CERES-BBR-ADMs using MODIS band 31. Retrieved fluxes are compared against apparent fluxes derived from CERES Terra ADMs.



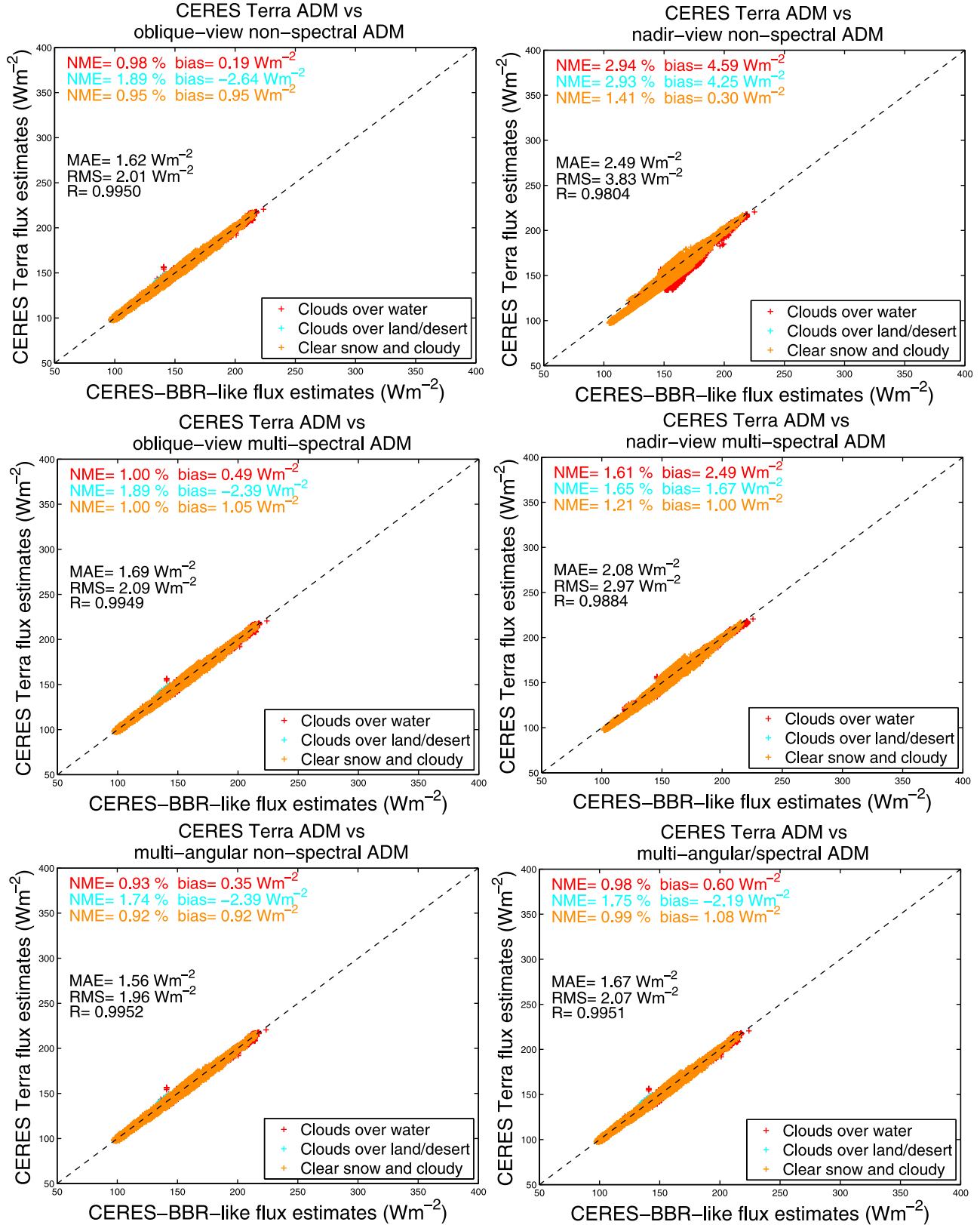


**Figure 13.** Evaluation of TOA fluxes estimated from LW CERES-BBR-ADMs using three MODIS thermal bands. Retrieved fluxes are compared against apparent fluxes derived from CERES Terra ADMs.

**Table 4.** Number of Scenes for Each CERES LW ADM ID Selected From the CERES-BBR-like Database

CERES ADM ID	Targets With One MODIS Band	Targets With Three MODIS Bands
Clouds over water	770 812	2 917
Clouds over land/desert	141 973	134
Clear snow and cloudy	372 074	79 430
Clear water	85 222	–
Clear land/desert	85 288	–
Clear mixed surface type	44 436	–

algorithm reduces the RMS error in 6% and 42% compared to the nonspectral oblique and nadir angular models, respectively. However, the methods based on the spectral dependence of the scene anisotropy show irregular results (Figure 12, middle left and bottom). The expected improvement employing one single MSI band is low although it can be theoretically measurable. However, the monospectral angular models applied over satellite data does not clearly improve the results achieved with the nonspectral models. The substantial difference between MAE and RMS errors obtained for the nadir view monospectral ADM indicates a significant variance in the individual errors of the sample. In particular, bright scenes with clouds over water (low cloud coverage) give NME errors and error dispersion higher than those obtained with the nadir view nonspectral model; however, lower errors are obtained for the rest of scenes types. The oblique view monospectral model does not increase the flux accuracy and show even slightly worse results than the nonspectral ADM.

### 3.5. Empirical Evaluation of CERES-BBR-ADMs Using CERES TAT and Three MODIS Channels

[44] The available data is greatly reduced when the error analysis is reprocessed to select only scenes with MODIS observations in the three required thermal bands. As a result the 96% of the data analyzed pertain to the clear snow and cloudy CERES LW ADM type (composed by sea ice, fresh and permanent snow over clear-sky and cloudy conditions). Consequently, the analysis becomes only meaningful for that specific scene type. In this case, high discrepancies between CERES-BBR and CERES Terra ADMs could be not attributable to CERES fluxes disparity, since CERES flux differences obtained for the clear snow and cloudy scene type are rather low (less than  $2 \text{ W m}^{-2}$ , see Table 6).

[45] Figure 13 shows results that partially agree with the model performance discussed in the theoretical error analysis (see section 2.2). As expected, the highest uncertainties are obtained for the nonspectral angular model which employs the nadir view in the flux retrieval (Figure 13, top right) while the oblique view model (Figure 13, top left) produces accurate results (RMSE around  $2 \text{ W m}^{-2}$ ). The flux accuracy improvement using the effective radiance instead of single views in the nonspectral models agrees with the results obtained in the simulations (Figure 13, bottom left). This ADM model accurately fits the thermal CERES flux retrievals reducing the RMS error in 49% and 3% compared to nadir view and oblique view nonspectral models, respectively. A small flux underestimation is observed for clouds over water and land scenes; however,

this is not significant because of the few data available for the scene type.

[46] The behavior of the nadir view multispectral model is coherent with the conclusions reached in the theoretical study (Figure 13, middle right). The multispectral ADM method that makes use of nadir observations highly improves the RMSE results of the nadir view nonspectral angular (23.6%). However, the accuracy increase using the oblique view in the multispectral ADM is not as evident as the simulations shown (Figure 13, middle left). This could be caused by a parallax problem in the CERES-BBR-like database whereby geolocation of nadir (MODIS) and oblique (CERES) views at the surface can result in displacements between nadir and oblique footprint centroids at cloud level by up to 20 km [Loeb *et al.*, 2002]. Since emission reaching the satellite for cloudy scenes is mostly from the top cloud, this introduces some discrepancy between nadir and oblique views. The multiangular/spectral model improves the error results and the correlation between CERES Terra and CERES-BBR fluxes achieved in the single-view spectral and nonspectral models but it does not show better accuracy than the one estimated with the multiangular nonspectral model (Figure 13, bottom right). It could be expected, a priori, a better result than that shown in the oblique view nonspectral models as it was discussed in the theoretical error analysis. But the problem detected in the oblique view multispectral model affects the accuracy of this methodology too. Thus, it cannot be concluded that the use of the effective radiance in the multispectral methodology contributes to increase the accuracy in the radiance-to-flux conversion of satellite-based data. However, it is important to remark that the errors given by these models are in between the range of the flux differences obtained between nadir and off-nadir CERES estimates in the CERES-BBR-like database. Thus, it is difficult to clearly distinguish from the different error sources.

## 4. Conclusions

[47] This paper studies the thermal radiance-to-flux conversion when BBR multidirectional  $\{L(\theta)\}_{BB}$  and MSI multispectral  $\{L(\lambda)\}_{NB}$  radiances are combined in the flux retrieval algorithm. The study is based on a large database construction of spectral radiance fields at TOA using plane parallel radiative transfer calculations. The commonly used SAB algorithms rely on the cloud remote sensing performance, hence the scene misidentification is necessary to be considered using bin classification. The methodology developed in the paper avoids this potential error source. Nevertheless, the empirical approach escapes from theoretical biases such as 3-D cloud effects (nonhomogeneous or

**Table 5.** CERES Instantaneous LW TOA Flux Uncertainties for Terra ADMs<sup>a</sup>

Region	Terra ADMs Error ( $\text{W m}^{-2}$ )	
	Clear Sky	All Sky
Tropics	3.3 (1.1)	5.1 (1.8)
Midlatitude	2.9 (1.0)	5.4 (2.3)
Polar	3.4 (1.6)	4.0 (2.0)

<sup>a</sup>Extracted from CERES Terra Edition2B SSF data quality summary document. Percentages are given in parentheses.

**Table 6.** Differences ( $\text{W m}^{-2}$ ) Between CERES Terra Flux Estimates Derived From Nadir and Oblique Views Averaged for the Scene Types Within the CERES-BBR-like Database<sup>a</sup>

CERES ADM ID	Bias, One MODIS Band	Bias, Three MODIS Bands
Clouds over water	3.83	3.24
Clouds over land/desert	4.71	5.22
Clear snow and cloudy	2.86	1.86
Clear water	1.97	—
Clear land/desert	3.29	—
Clear mixed surface type	3.72	—

<sup>a</sup>The CERES flux differences are separately obtained for scenes with one or three MODIS thermal bands available.

broken cloud fields) and unknown ice crystal scattering. However, the BBR-RT database employed is still representative of the anisotropy because of surface temperature, surface emissivity, atmospheric constituents, cirrus, stratus and multilayer cloud covers.

[48] An independent theoretical error analysis was performed to evaluate the ADMs. The LW BBR-ADMs were applied over a radiance data set constructed with the RT code employed in the algorithm development and following the same physical restrictions used in the original inputs. The analysis shows that the combination of multiangular BBR observations into a modeled effective radiance provides a new quantity that improves the radiance-to-flux inversion. The weak correlation between radiances and the spectral behavior of the radiation field can also be exploited to decrease the thermal flux retrieval error. Finally, the combination of both methodologies is shown to be able to reduce the error in the flux conversion with respect to single-view and nonspectral based ADM conversion schemes.

[49] Nevertheless, it is difficult to extrapolate theoretical results to real situations because of the insufficient or biased parameter sampling during the database construction. Thus, in the second part of the paper, the LW BBR ADMs are evaluated against the CERES Terra flux retrieval algorithms. The ADM BBR methodology is instrument dependent, thus new angular dependence models are constructed for the CERES instrument in order to apply the methodology over the sensors on board the Terra platform. Prior to the empirical evaluation, those theoretical models are successfully validated with a RT database.

[50] A large database of CERES TAT radiance measurements is collected for the study. However, the number of potentially fully useful satellite data is much lower than expected. The BBR models are successfully applied over the CERES database and most of the theoretical achievements are verified according to the conclusions extracted. Consequently, the empirical results are consistent with the assumptions taken in the description of the methodology; however, the multiangular/spectral model cannot be fully tested because of limitations in the comparison and the CERES database. Considering that the limitations on the satellite database due to the lack of coincident CERES TAT observations and MODIS radiances (at channels 29, 31 and 32) in SSF data could mask the real results, more data with increased variety of scene types would be required in order to complete the analysis and reach more significant conclusions in the comparison.

[51] The multiangular/spectral ADM is the angular model that better exploits the synergy between BBR and MSI instruments, making use in the same algorithm of both multiangular and multispectral EarthCARE capabilities. According to the theoretical error analysis the multiangular/spectral model can deliver thermal flux estimates with errors up to  $0.4 \text{ W m}^{-2}$ . This result improves the accuracy of the single-view nonspectral models in 90% and 32% with respect to nadir and oblique views, respectively. The empirical validation study carried out for the multiangular/spectral model provides MAE and RMSE values of 1.7 and  $2.1 \text{ W m}^{-2}$ , respectively.

[52] **Acknowledgments.** The authors would like to thank Bernhard Mayer and Ulrich Hamann of DLR for their help in the use of the LibRadtran model, Nicolas Clerbaux of RMIB for his constructive comments on the LW GERB flux operational retrieval algorithm, and Luis Guanter of FUB and the anonymous reviewers for their useful advice and suggestions. They are also grateful to the Atmospheric Sciences Data Center (ASCD) at NASA Langley Research Center and EUMETSAT for providing the CERES and MetOp-A data, respectively. The MODIS and AVHRR band spectral responses were provided by the MODIS Characterization Support Team and the NOAA National Climate Data Center (NCDC).

## References

- Anderson, G. P., S. A. Clough, F. X. Kneizys, J. H. Chetwynd, and E. P. Shettle (1986), AFGL atmospheric constituent profiles (0–120 km), technical report, Opt. Phys. Div., Air Force Geophys. Lab., Hanscom AFB, Mass.
- Berk, A., L. Bernstein, G. Anderson, P. Acharya, D. Robertson, J. Chetwynd, and S. Adler-Golden (1998), MODTRAN cloud and multiple scattering upgrades with application to AVIRIS, *Remote Sens. Environ.*, **65**, 367–375.
- Bodas-Salcedo, A., J. Gimeno-Ferrer, and E. López-Baeza (2003), Flux retrieval optimization with a nonscanner along-track broadband radiometer, *J. Geophys. Res.*, **108**(D2), 4061, doi:10.1029/2002JD002162.
- Boylana, J. W., and A. G. Russell (2006), PM and light extinction model performance metrics, goals, and criteria for three-dimensional air quality models, *Atmos. Environ.*, **40**, 4946–4959.
- Capderou, M., and M. Viollier (2006), True along-track scan to improve radiation budget estimations, *J. Atmos. Oceanic Technol.*, **23**, 1093–1103, doi:10.1175/JTECH1907.1.
- Chevallier, F., F. Cheruy, N. A. Scott, and A. Chedin (1998), A neural network approach for a fast and accurate computation of a longwave radiative budget, *J. Appl. Meteorol.*, **37**, 1385–1397.
- Chevallier, F., J.-J. Morcrette, A. Chedin, and F. Cheruy (2000), TIGR-like atmospheric-profile databases for accurate radiative-flux computation, *Q. J. R. Meteorol. Soc.*, **126**, 777–785.
- Clerbaux, N., S. Dewitte, L. Gonzalez, C. Bertrand, B. Nicula, and A. Ipe (2003), Outgoing longwave flux estimation: Improvement of angular modelling using spectral information, *Remote Sens. Environ.*, **85**, 389–395.
- Clerbaux, N., J. Russell, S. Dewitte, C. Bertrand, D. Capron, B. D. Paepe, L. G. Sotolino, A. Ipe, R. Bantges, and H. Brindley (2009), Comparison of GERB instantaneous radiance and flux products with CERES edition-2 data, *Remote Sens. Environ.*, **113**, 102–114, doi:10.1016/j.rse.2008.08.016.
- Domenech, C., D. P. Donovan, H. W. Barker, M. Bouvet, and E. Lopez-Baeza (2007), Improvement of broadband radiance to flux conversion by using the synergy between active and passive remote sensing instruments, in *Remote Sensing of Clouds and the Atmosphere XII*, vol. 6745, edited by A. Comerón et al., p. 67450Z, Int. Soc. for Opt. Eng., Bellingham, Wash., doi:10.1117/12.738156.
- Domenech, C., E. Lopez-Baeza, D. P. Donovan, and T. Wehr (2011), Radiative flux estimation from BBR using synthetic angular models in the EarthCARE mission framework. Part I: Methodology, *J. Appl. Meteorol. Clim.*, doi:10.1175/2010JAMC2526.1, in press.
- EarthCARE Mission Advisory Group (2006), Earth Clouds, Aerosols and Radiation Explorer (EarthCARE) mission requirements document, *Rep. EOP-SM/1567/TW*, Eur. Space Agency, Paris.
- European Space Agency (2004), Reports for mission selection, the six candidate Earth Explorer missions. EarthCARE—Earth Clouds, Aerosols and Radiation Explorer, *Eur. Space Agency Spec. Publ.*, SP-1279(1).

- Harries, J. E., et al. (2005), The Geostationary Earth Radiation Budget project, *Bull. Am. Meteorol. Soc.*, **86**, 945–960, doi:10.1175/BAMS-86-7-945.
- Kandel, R., M. Viollier, P. Raberanto, J. P. Duvel, L. A. Pakhomov, V. A. Golovko, A. P. Trishchenko, J. Mueller, E. Raschke, R. Stuhlmann, and the International ScaRaB Scientific Working Group (ISSWG) (1998), The ScaRaB Earth Radiation Budget dataset, *Bull. Am. Meteorol. Soc.*, **79**, 765–783.
- Key, J. R., P. Yang, B. A. Baum, and S. L. Nasiri (2002), Parameterization of shortwave ice cloud optical properties for various particle habits, *J. Geophys. Res.*, **107**(D13), 4181, doi:10.1029/2001JD000742.
- Loeb, N. G., S. Kato, and B. A. Wielicki (2002), Defining top-of-the-atmosphere flux reference level for Earth Radiation Budget studies, *J. Clim.*, **15**, 3301–3309.
- Loeb, N. G., N. M. Smith, S. Kato, W. F. Miller, S. K. Gupta, P. Minnis, and B. A. Wielicki (2003), Angular distribution models for top-of-atmosphere radiative flux estimation from the Clouds and the Earth's Radiant Energy System instrument on the Tropical Rainfall Measuring Mission satellite. Part I: Methodology, *J. Appl. Meteorol.*, **42**, 240–265.
- Loeb, N. G., S. Kato, K. Loukachine, and N. Manalo-Smith (2005), Angular distribution models for top-of-atmosphere radiative flux estimation from the Clouds and the Earth's Radiant Energy System instrument on the Terra satellite. Part I: Methodology, *J. Atmos. Oceanic Technol.*, **22**, 338–351.
- Loeb, N. G., S. Kato, K. Loukachine, N. Manalo-Smith, and D. R. Doelling (2007), Angular distribution models for top-of-atmosphere radiative flux estimation from the Clouds and the Earth's Radiant Energy System instrument on the Terra satellite. Part II: Validation, *J. Atmos. Oceanic Technol.*, **24**, 564–584, doi:10.1175/JTECH1983.1.
- Mayer, B., and A. Kylling (2005), The LibRadtran software package for radiative transfer calculations—Description and examples of use, *Atmos. Chem. Phys.*, **5**(7), 1855–1877.
- Minnis, P., and M. M. Khaiyer (2000), Anisotropy of land surface skin temperature derived from satellite data, *J. Appl. Meteorol.*, **39**, 1117–1129.
- Otterman, J., D. Starr, T. Brakke, R. Davies, H. Jacobowitz, and A. Mehta (1997), Modeling zenith-angle dependence of outgoing longwave radiation: Implication for flux measurement, *Remote Sens. Environ.*, **62**, 90–100.
- Pierluissi, J. H., and G.-S. Peng (1985), New molecular transmission band models for lowtran, *Opt. Eng.*, **24**, 541–547.
- Ricchiazzi, P., S. Yang, C. Gautier, and D. Sowle (1998), SBDART: A research and teaching software tool for plane-parallel radiative transfer in the Earth's atmosphere, *Bull. Am. Meteorol. Soc.*, **79**, 2101–2114.
- Stamnes, K., S. C. Tsay, W. Wiscombe, and K. Jayaweera (1988), Numerically stable algorithm for discrete-ordinate-method radiative transfer in multiple scattering and emitting layered media, *Appl. Opt.*, **27**, 2502–2509.
- Stubenrauch, C. J., J.-P. Duvel, and R. S. Kandel (1993), Determination of longwave anisotropic emission factors from combined broad- and narrowband radiance measurements, *J. Appl. Meteorol.*, **32**, 848–856.
- Suttles, J. T., R. N. Green, P. Minnis, G. L. Smith, W. F. Staylor, B. A. Wielicki, I. J. Walker, D. F. Young, V. R. Taylor, and L. L. Stowe (1988), Angular radiation models for Earth-atmosphere system, vol. 1, Shortwave radiation, *NASA Ref. Publ.*, **RP-1184**.
- Suttles, J. T., R. N. Green, G. L. Smith, B. A. Wielicki, I. J. Walker, V. R. Taylor, and L. L. Stowe (1989), Angular radiation models for Earth-atmosphere system, vol. 2, Longwave radiation, *NASA Ref. Publ.*, **RP-1184**.
- Viollier, M., C. Standfuss, O. Chomette, and A. Quesney (2009), Top-of-atmosphere radiance-to-flux conversion in the SW domain for the ScaRaB-3 instrument on megha-tropiques, *J. Atmos. Oceanic Technol.*, **26**, 2161–2171.
- Wang, J., W. Rossow, and Y.-C. Zhang (2000), Cloud vertical structure and its variations from a 20-year global rawinsonde dataset, *J. Clim.*, **13**, 3041–3056.
- Wielicki, B. A., B. R. Barkstrom, E. F. Harrison, R. B. Lee III, G. L. Smith, and J. E. Cooper (1996), Clouds and the Earth's Radiant Energy System (CERES): An Earth observing system experiment, *Bull. Am. Meteorol. Soc.*, **77**, 853–868.
- Wilber, A. C., D. Kratz, and S. Gupta (1999), Surface emissivity maps for use of satellite retrievals of longwave radiation, *NASA Tech. Publ.*, **TP-99-209362**.
- Yang, P., K. Liou, K. Wyser, and D. Mitchell (2000), Parameterization of the scattering and absorption properties of individual ice crystals, *J. Geophys. Res.*, **105**, 4699–4718.

C. Domenech and J. Fischer, Institute for Space Sciences, Free University of Berlin, Berlin D-12165, Germany. (carlos.domenech@wew.fu-berlin.de; juergen.fischer@wew.fu-berlin.de)

T. Wehr, Mission Science Division, Atmospheric Section, ESTEC, European Space Agency, NL-2200 AG Noordwijk ZH, Netherlands. (tobias.wehr@esa.int)